1
2

Single fluorogen imaging reveals distinct environmental and structural features of biomolecular condensates

3
4

Authors: Tingting Wu[1,2,4], Matthew R. King[2,3,4], Yuanxin Qiu[1,2], Mina Farag[2,3], Rohit V. Pappu[2,3*], Matthew D. Lew[1,2*]

5

Affiliations:

6
7
8

[1] Department of Electrical and Systems Engineering, Washington University in St. Louis, James F. McKelvey School of Engineering, Washington University in St. Louis; St. Louis, MO 63130, USA.

9
10

[2] Center for Biomolecular Condensates, James F. McKelvey School of Engineering, Washington University in St. Louis; St. Louis, MO 63130, USA.

11
12

[3] Department of Biomedical Engineering, Washington University in St. Louis, James F. McKelvey School of Engineering, Washington University in St. Louis; St. Louis, MO 63130, USA.

13

[4]These authors contributed equally: Tingting Wu, Matthew R. King

14

Corresponding authors. Email: pappu@wustl.edu; mdlew@wustl.edu

15

16

Abstract:

17
18
19
20
21
22
23
24
25
26
27
28
29
30

Biomolecular condensates are viscoelastic materials. Simulations predict that fluid-like condensations are defined by spatially inhomogeneous organization of the underlying molecules. Here, we test these predictions using single-fluorogen tracking and super-resolution imaging. Specifically, we leverage the localization and orientational preferences of freely diffusing fluorogens and the solvatochromic effect whereby specific fluorogens are turned on in response to condensate microenvironments. We deployed three different fluorogens to probe the microenvironments and molecular organization of different protein-based condensates. The spatiotemporal resolution and environmental sensitivity afforded by single-fluorogen imaging shows that the internal environments of condensates are more hydrophobic than coexisting dilute phases. Molecules within condensates are organized in a spatially inhomogeneous manner, and this gives rise to slow-moving nanoscale molecular clusters that coexist with fast-moving molecules. Fluorogens that localize preferentially to the interface help us map their distinct features. Our findings provide a structural and dynamical basis for the viscoelasticity of condensates.

Main Text

Biomolecular condensates are thought to provide spatial and temporal control over cellular matter [1]. Proteins with intrinsically disordered regions (IDRs) such as prion-like low complexity domains (PLCDs) and arginine-glycine-rich (RG-rich) regions are prominent drivers of different types of condensates [2, 3]. Several investigations have suggested that simple, single-component condensates formed by PLCDs and RG-rich IDRs and complex multicomponent condensates such as nucleoli and the mitochondrial nucleoid[4] are viscoelastic materials [5, 6, 7, 8, 9, 10]. Viscoelastic materials should feature network-like internal structures [11, 12]. The dynamical rearrangement of these networks and the transport properties of the underlying molecules should determine whether the long-time behaviors of viscoelastic materials are dominantly viscous (fluid-like) or elastic (solid-like) [10]. Despite the central importance of nano- and mesoscale organization of molecules to condensate viscoelasticity, these details remain elusive even within simple one-component condensates.

Recent computational studies have predicted that within simple, one-component condensates formed by PLCDs, the protein molecules organize to form spatially inhomogeneous networks [13, 14] (**Fig. 1a**). Results from simulations suggest that internal networks in condensates have dynamic, hub-and-spoke organization with hubs being nanoscale clusters of molecules that are generated by reversible physical crosslinks among molecules [13, 14]. Here, we report results from experimental tests of computational predictions using single-molecule tracking and single-molecule orientation localization microscopy (SMOLM). In these experiments, we combine freely diffusing fluorogenic probes [15, 16, 17] with single-molecule imaging [18, 19, 20, 21, 22, 23] to characterize the internal solvent properties as well as the organization and dynamics of molecules within condensates.

Environmentally sensitive dyes change their fluorescence intensity (making them fluorogens) or color (making them solvatochromic) based on their microenvironment (**Extended Data Fig. 1**) [15, 16, 17, 24, 25, 26, 27]. We deployed fluorogenic molecules that are solvatochromic and used them as structural probes in super-resolution single-molecule imaging to investigate condensates formed by three sequence variants of the PLCD of hnRNP-A1 (A1-LCD) [2, 28] and the RG-rich IDR from the protein DDX4 [3, 29]. We focused on condensates formed by single proteins to test the structural basis for measured viscoelastic properties [7, 30, 31] and predictions that have emerged from physical theory and computations [13, 14, 32].

In separate measurements we used different polarity-sensing fluorogens namely, Nile blue (NB), Nile red (NR) [15, 16], and merocyanine 540 (MC540)[17]. These fluorogens are dark in aqueous solutions, even when they are pumped with an excitation laser. As the fluorogens diffuse through solution, they can either partition into hydrophobic environments or bind specifically to hydrophobic pockets within or outside condensates. This binding causes an increase in their fluorescence quantum yield and a shift in their absorption and emission spectra, termed solvatochromism (**Fig. 1a**).

NR (**Fig. 1b, (i)**) is minimally soluble in aqueous buffers, and it has a solubility of 280 μM (0.09 mg/ml) in a 1:10 mixture of DMSO (dimethyl sulfoxide) and phosphate buffered saline (PBS). In contrast, NB (**Fig. 1b, (ii)**), which is essentially the same as NR, albeit with an amine, has a solubility in water of 0.14 M (50 g/l). MC540 (**Fig. 1b, (iii)**) partitions to interfaces between membranes and aqueous environments [17]. Interiors of condensates are likely to be microenvironments that are distinct from the coexisting phases [4, 8, 13, 14, 33, 34] that are delineated by

75   interfaces. Therefore, we used MC540 as a probe of condensate interfaces. Note that none of the
76   proteins are chemically modified by dyes or other tags. Instead, the fluorogenic dyes, which are
77   present at low micromolar or sub-micromolar concentrations in single-molecule measurements,
78   freely diffuse in solution and through the condensates [35].
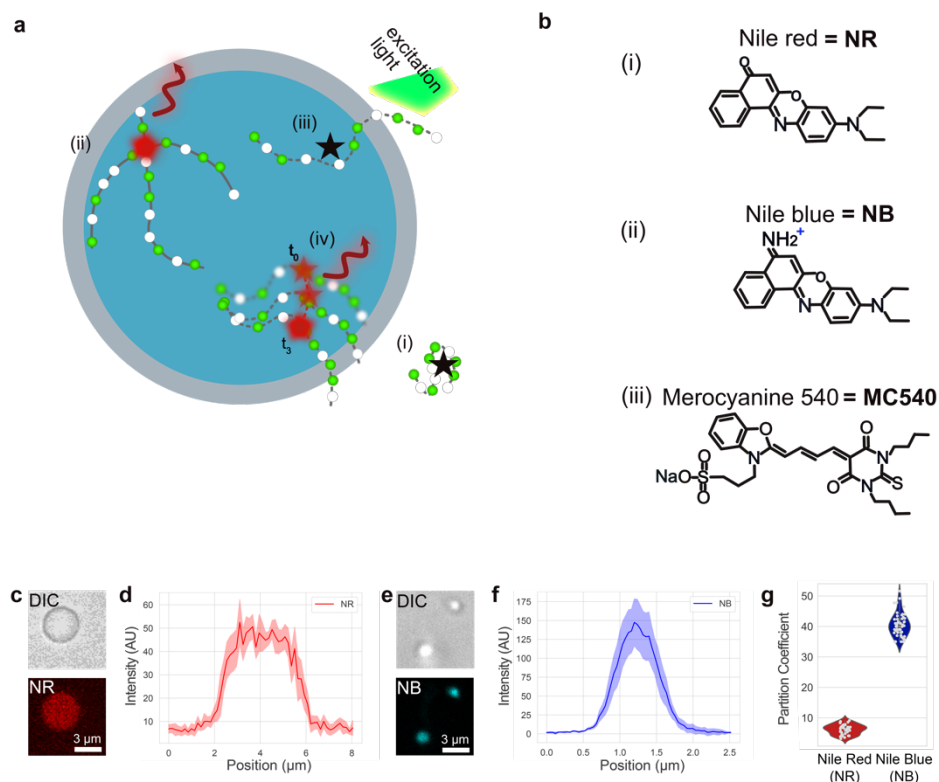
79

80

81   **Fig. 1. Details of fluorogenic probes and their partitioning into biomolecular condensates. a**: As fluorogens
82   (shown as black stars) diffuse through solution, they encounter different chemical environments in the dilute phase
83   (white space), in the condensate (blue circle), and in the interface between the dilute phase and condensate (gray
84   region). In response, they either (i, iii) remain dark (black stars) or (ii, iv) become fluorescent (red stars and curved
85   arrows). Their (ii, iv) speeds of movement and brightness are also affected. **b**: Chemical structures of the three different
86   fluorogens used for imaging condensates: (i) Nile red (NR), (ii) Nile blue (NB), and (iii) merocyanine 540 (MC540).
87   (c) Condensates formed by unlabeled A1-LCD molecules were imaged using differential interference contrast (DIC)
88   microscopy. NR partitions into these condensates (signal shown in the red channel). (d) Point scanning confocal
89   microscopy was used to quantify the partition coefficients of NR into A1-LCD condensates. (e) DIC images of A1-
90   LCD condensates and confocal images showing the partitioning of NB into these condensates. (f) Point scanning
91   confocal microscopy was used to quantify the partition coefficients of NB into A1-LCD condensates. (g) Partition
92   coefficients for NR and NB measured using partitioning data gathered from ~50 different condensates. The median
93   values are 6.5 and 40 for NR and NB, respectively.

94   Prior to deploying the fluorogens as imaging probes within condensate interiors, we used
95   point scanning confocal microscopy to measure the partitioning of NR and NB into condensates
96   formed by wild-type A1-LCD (**Fig. 1c-1f**). The partitioning measurements were performed using
97   34 µM NR and 40 µM NB. Across ~50 distinct measurements we obtain median values of 6.5 and
98   40 for the partition coefficients of NR and NB into A1-LCD-rich phases (**Fig. 1g**). The partition
99   coefficient of NB is eight times higher than that of NR. In the single-molecule measurements, we
100 use concentrations of 3.4 µM for NR and 2 nM for NB. Based on the measured partition

3

101   coefficients, the inferred concentration for NR and NB in the dense phase would be 17 µM and
102   0.08 µM, respectively. Therefore, the concentrations of NR and NB in the dense phase are well
103   below the threshold concentrations that define their solubility limits phase separation in aqueous
104   solvents.

105   We also asked if the fluorogens function as ligands that alter the driving forces for phase
106   separation of the macromolecules. Ligands that stabilize dense phases will lower the
107   macromolecular saturation concentration (c_{sat}) whereas ligands that destabilize dense phases will
108   have the opposite effect [36, 37]. We measured the effects of fluorogens on the c_{sat} values of A1-LCD
109   molecules. These measurements were performed at two different temperatures and different bulk
110   concentrations of each of the dyes. The data show that effects of the dyes on the c_{sat} are negligible,
111   being within the narrow errors of the measured c_{sat} values in the absence of the dyes (**Extended
112   Data Fig. 2a-b**). Therefore, the fluorogenic and solvatochromic dyes are non-perturbative when
113   used at single-molecule imaging concentrations. The control measurements establish that the
114   features we extract from single-molecule measurements are direct consequences of interactions of
115   the dyes with the macromolecules and not a consequence of the interactions of the dyes with
116   themselves.

117   **Single-molecule imaging shows that spatial inhomogeneities extend down to the nanoscale.**

118   We leveraged the diffusion and transient binding of NB and NR [35, 38] as a photo-switching
119   ("blinking") mechanism for super-resolution, single-molecule localization microscopy (SMLM)
120   [39, 40, 41, 42]. As individual probes diffuse through solution, they remain dark until they encounter
121   hydrophobic environments or bind to hydrophobic sites. Within hydrophobic pockets, they become
122   bright, and if they are sufficiently immobilized within the pocket (e.g., ~10 ms—the timescale of
123   the camera integration time), then enough fluorescence signal can be accumulated to detect and
124   localize single fluorogens. The fluorogens become dark when they leave hydrophobic pockets [18].
125   Accumulating the positions of many blinking events yields detailed SMLM maps of internal
126   structures within condensates with nanoscale resolution and single-molecule sensitivity (**Movie
127   S1**).

128   Super-resolution images of single condensates show that both NR and NB exhibit non-
129   uniform localization patterns (**Fig. 2a, 2b**). We measured digital on / off blinking of the fluorogens
130   within apparent "hotspots" that are formed by the macromolecules within condensates. The
131   hotspots are repeated "bursts" of single-molecule fluorescence turning on and off via binding and
132   unbinding / photobleaching. Based on the observations in computations [13], we refer to the hotpots
133   as hubs. We observed hubs at the nanoscale in SMLM images collected using both NR and NB
134   (**Fig. 2c**). To quantify the spatial inhomogeneity using single-molecule blinking (**Fig. 2d**), we
135   calculated the excess variance of the number of single-fluorogen localizations within a spatial pixel
136   within each condensate (see Methods). If a fluorogenic probe has a uniform probability of blinking
137   across the entire condensate, e.g., in the absence of any hotspots, then its localization density would
138   be Poisson-distributed [43]. This behavior yields an excess variance of zero (**Fig. S3**). The
139   condensates imaged sequentially by NB and NR showed larger than expected variances with a
140   mean excess variance of 1.3 ± 0.8 (std. dev., 2.1×10^4 localizations/condensate on average). Thus,
141   SMLM shows that both NB and NR exhibit large and significant spatial variations in their blinking
142   dynamics (**Fig. 2d**).

143   The super-resolution images of NR show the presence of nanoscale hubs (**Fig. 2c**). Next,
144   we measured the relative proportion of localizations that are spatially clustered to quantify the

145   relative affinities of NR and NB for localizing to nanoscale hubs (**Fig. 2e, 2f**). Our analysis is
146   motivated by theories showing that density fluctuations are useful order parameters to assay for
147   density inhomogeneities [44]. For each localization, we compared the local and surrounding density
148   and then computed a clustering coefficient [45, 46]. Molecules with clustering coefficients above a
149   threshold of 20 are classified as being clustered (**Fig. 2e**, see Methods). For the five condensates
150   imaged by NR and NB, 27% ± 3% of NR molecules and 13% ± 4% of NB molecules were clustered.
151   This indicates that clustering is detected twice as often with NR when compared to NB. The
152   implication is that while both probes exhibit a strong affinity to hubs, NR localizes more strongly
153   to nanoscale clusters than NB.

154   Next, we quantified the similarities and differences between spatial inhomogeneities
155   mapped by NR and NB [47, 48]. For images collected using both NR and NB, we found that the
156   diffuse regions, characterized by small relative single-fluorogen localization densities, are mostly
157   uncorrelated, i.e., random. However, regions exhibiting high NR and NB blinking events are
158   highly correlated with one another (**Extended Data Fig. 4**). These data suggest that the affinities
159   and binding lifetimes of the fluorogens at hubs are dye-specific, but the hubs identified by the dyes
160   are equivalent.

161
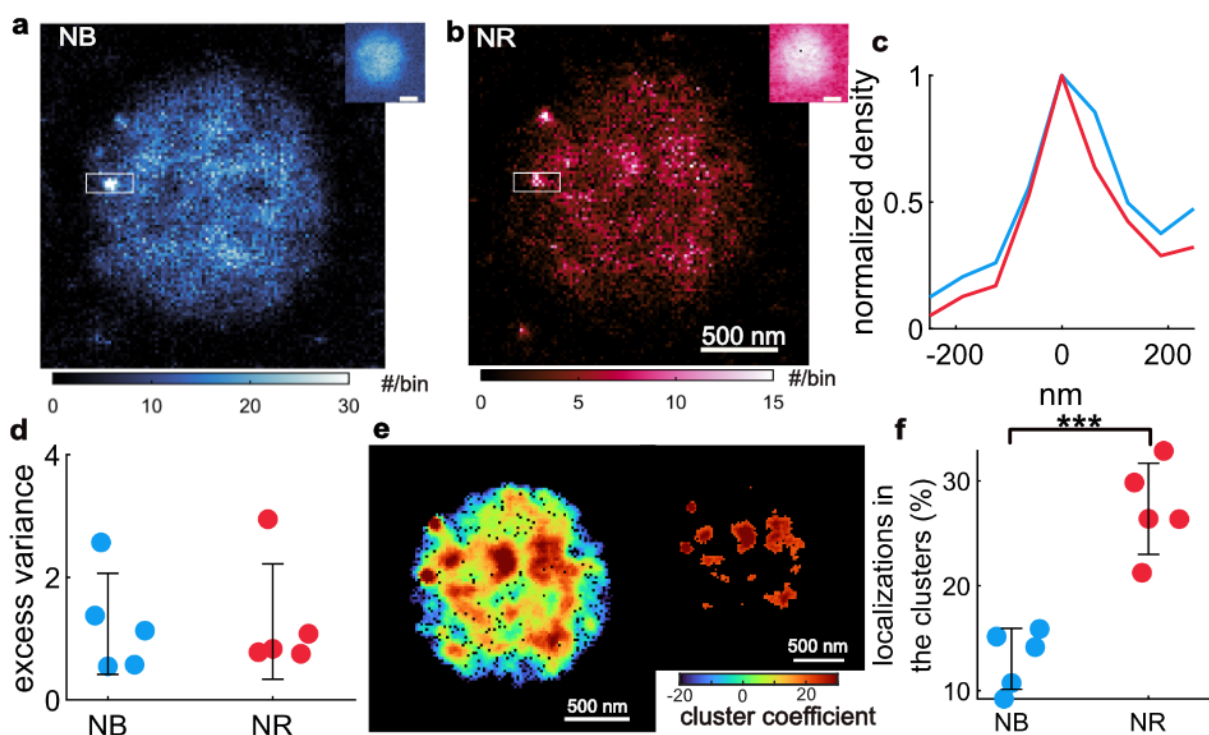
Fig. 2. Single molecule localization microscopy (SMLM) of NB and NR reveals that they bind to molecules that are organized into nanoscale clusters within condensates. a, **b**: SMLM images of a single A1-LCD condensate collected using (**a**) NB and (**b**) NR. Top insets: epifluorescence images. Color bars: number (#) of single-molecule localizations within each 20 nm × 20 nm bin. **c**: Localization profile along the long axis of the white box shown in (**a**, **b**). **d**: Quantifying the binding and activation of NB (blue) and NR (red) within five condensates using excess variance. Larger excess variance values represent greater heterogeneities in the blinking statistics of fluorogenic probes within a condensate; zero excess variance represents uniform blinking statistics throughout the condensate. **e**: A1-LCD condensate in (**b**) imaged by NR and color-coded by clustering coefficient; molecules with clustering coefficients

5

171   above a threshold of 20 are classified as being clustered. Inset: map of regions that contain clustered NR localizations.
172   **f**: Percentages of single-molecule localizations that are spatially clustered for five condensates.

Single-molecule tracking shows slow moving nanoscale hubs that coexist with fast moving molecules.

175   Our data indicate that nanoscale hubs represent clusters of proteins that define distinctive
176   local environments. Single-molecule imaging also shows that nanoscale hubs within each of the
177   condensates disappear from one location and reappear at nearby locations (**Movies S2 and S3**).
178   We probed these dynamics inside condensates by tracking the movements and fluorescence burst
179   durations of individual fluorogens (**Movie S4**). The burst duration t_b is correlated with the amount
180   of time a fluorogen spends in a fluorescence-promoting environment. The speed measures the
181   distance covered by a fluorogen within 10 ms intervals (**Fig. 3a**, **Extended Data Fig. 5**). As a
182   fluorogen explores a condensate, changes in the local environment cause both its burst duration
183   and speed of movement to vary. For example, the burst durations of NR range from 10 ms to more
184   than 170 ms (**Fig. 3b**). This heterogeneity is highlighted by reconstructing SMLM images using
185   only single molecules with short burst durations ($t_b \leq 60$ ms, **Fig. 3c**) versus those with long burst
186   durations ($t_b > 60$ ms, **Fig. 3d**). Single molecules with short burst durations are distributed
187   uniformly across the condensate, while hotspots are dominant in the long-burst duration images.
188   This trend was also observed when the condensates were imaged using NB (**Extended Data Fig.**
189   **5i-5k**). However, when compared to NR, NB exhibits larger displacements (**Extended Data Fig.**
190   **5b,5d**). These data are consistent with the observation that the NB dyes localize to equivalent hubs
191   within condensates but their dwell times at the hubs are different from those of NR.

192   We separated NB emitters into three categories based on their speeds that were measured
193   between consecutive frames (10 ms exposure times, **Fig. 3e**). An SMLM image, reconstructed
194   from high-speed emitters, shows a uniformly distributed localization density across the condensate
195   (**Fig. 3f**). These fluorogens were localized within sufficiently hydrophobic environments to emit
196   fluorescence but bind relatively weakly, resulting in relatively high speeds. An SMLM image
197   reconstructed solely from low-speed emitters exhibits clusters and nonuniform localization
198   patterns (**Fig. 3g**). This phenomenon is consistent across six different A1-LCD condensates where
199   the average excess variance of single-molecule images reconstructed using emitters with low,
200   medium, and high speeds of emitters are 0.84 ± 0.33, 0.13 ± 0.06, and 0.05 ± 0.04, respectively
201   (**Fig. 3h**). Condensates imaged using NR showed similar trends (**Extended Data Fig. 5e-5g**).
202   Overall, NR and NB emitters with longer burst durations tend to have lower speeds (**Fig. 3i**). The
203   hubs revealed by longer-burst emitters and those sensed by slowly moving emitters are consistent
204   with one another (**Fig. 3** and **Extended Data Fig. 5**).

205   To provide a physical interpretation for why NR and NB dyes are trapped for longer periods
206   of time at hubs, we analyzed published results from lattice-based LaSSI simulations [13]. PLCDs are
207   linear associative biopolymers featuring cohesive motifs known as stickers that are interspersed
208   by solubility-determining spacers [49]. Interactions for A1-LCD and related PLCDs follow a
209   hierarchy whereby interactions between aromatic residues are the strongest [13]. Stickers form
210   reversible physical crosslinks with one another, whereas spacers modulate sticker-sticker
211   interactions and the coupling between phase separation and percolation [49, 50]. Aromatic residues of
212   A1-LCD and related PLCDs function as stickers that enable physical crosslinking of these
213   molecules [2, 28]. Conversely, charged, and polar residues interspersed between the stickers act as
214   spacers [2, 28]. The simulations of Farag et al.[13] showed that the spatial inhomogeneity and network

215 connectivity within PLCD condensates are governed by the valence of stickers [28] and differences
216 in interaction strengths between different stickers and spacers [13].
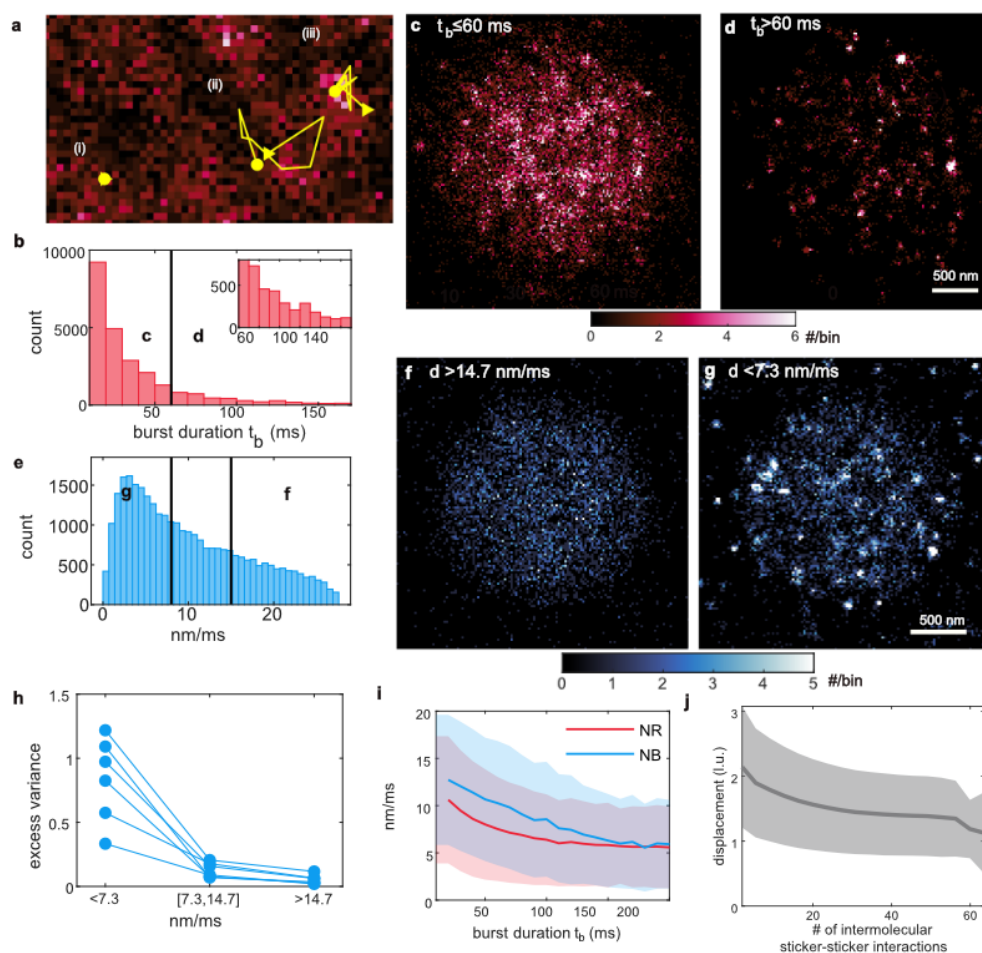
Fig. 3. Tracking of single-molecule fluorescence burst durations and speeds uncover inhomogeneous molecular organization and dynamics within condensates. a: Single NR fluorophores exhibit both (**i**) short and (**ii, iii**) long burst durations, as well as (**ii**) high and (**iii**) low speeds. **b:** burst duration t_b of NR. **c, d:** SMLM images of NR molecules with burst durations (**c**) shorter than 60 ms and (**d**) longer than 60 ms. **Extended data Fig. 5 j-k** shows burst duration data for NB. **e:** Speed distribution of NB measured between consecutive camera frames (10 ms exposure time). **f, g:** SMLM images of NB molecules with speeds (**f**) larger than 14.7 nm/ms and (**g**) smaller than 7.3 nm/ms. **Extended data Fig. 5 e-g** shows speed data for NR. **h:** Excess variance of NB localizations grouped by speeds (left: <7.3 nm/ms, middle: between 7.3/ms and 14.7 nm/ms, right: >14.7 nm/ms). Blue lines: excess variance of NB within each condensate. **i:** Speeds of NB (blue) and NR (red) as a function of their fluorescence burst durations. Lines: mean value averaged over 150,000 trajectories for NB and 129,000 trajectories for NR; shaded region: ±1 standard deviation. **j:** Displacement in lattice units (l.u.) of each chain within a simulated A1-LCD condensate as a function of the number of intermolecular sticker-sticker interactions. Results are from lattice-based Monte Carlo simulations [13].

229 We propose that the nanoscale hubs uncovered using NR and NB are direct readouts of
230 networked A1-LCD molecules formed via reversible, intermolecular physical crosslinks among
231 aromatic stickers. Accordingly, we probed the correlation between molecular displacements and
232 the extent of crosslinking in the simulated condensates. These simulations show that A1-LCD
233 molecules that are part of densely crosslinked networks have smaller overall displacements (**Fig.
234 3j**). The simulations suggest that nanoscale hubs observed using single fluorogen imaging are
235 clusters of A1-LCD molecules defined by the extent of physical crosslinking. The fluorogens
236 become trapped for longer times in nanoscale hubs because of the higher local density of stickers

7

237   within the clusters that underlie the hubs. Observations of dynamical inhomogeneities (**Fig. 3**) are
238   a consequence of spatial inhomogeneities (**Fig. 2**). Similar reports for dynamical inhomogeneities
239   arising from spatial inhomogeneities have been made by Shen et al.[51] using adaptive single-
240   molecule tracking in condensates that form at the post-synaptic density. Likewise, computations
241   that reproduce structure factors from small-angle neutron scattering measurements also show
242   spatial and dynamical inhomogeneities. Taken together with the work for Shen et al., [51] and Dar
243   et al.,[52] it appears that dynamical inhomogeneities within condensates are likely to be the
244   signatures of spatial inhomogeneities that result from phase separation coupled to percolation [50].

245   **Valence of aromatic residues impacts nanoscale dynamics of PLCDs within condensates.**

246   The driving forces for phase separation of A1-LCD and designed variants thereof are
247   governed by valence, i.e., the number and types of aromatic residues [2, 28]. We used NR and NB
248   dyes to obtain comparative assessments of nanoscale structures within condensates formed by two
249   variants of the A1-LCD system designated as Aro$^+$ and Aro$^-$ [28]. The Aro$^+$ variant has more
250   aromatic residues dispersed uniformly along the linear sequence when compared to the wildtype
251   A1-LCD, while the Aro$^-$ has fewer aromatic groups [28] (**Fig. 4a, Table S1**).
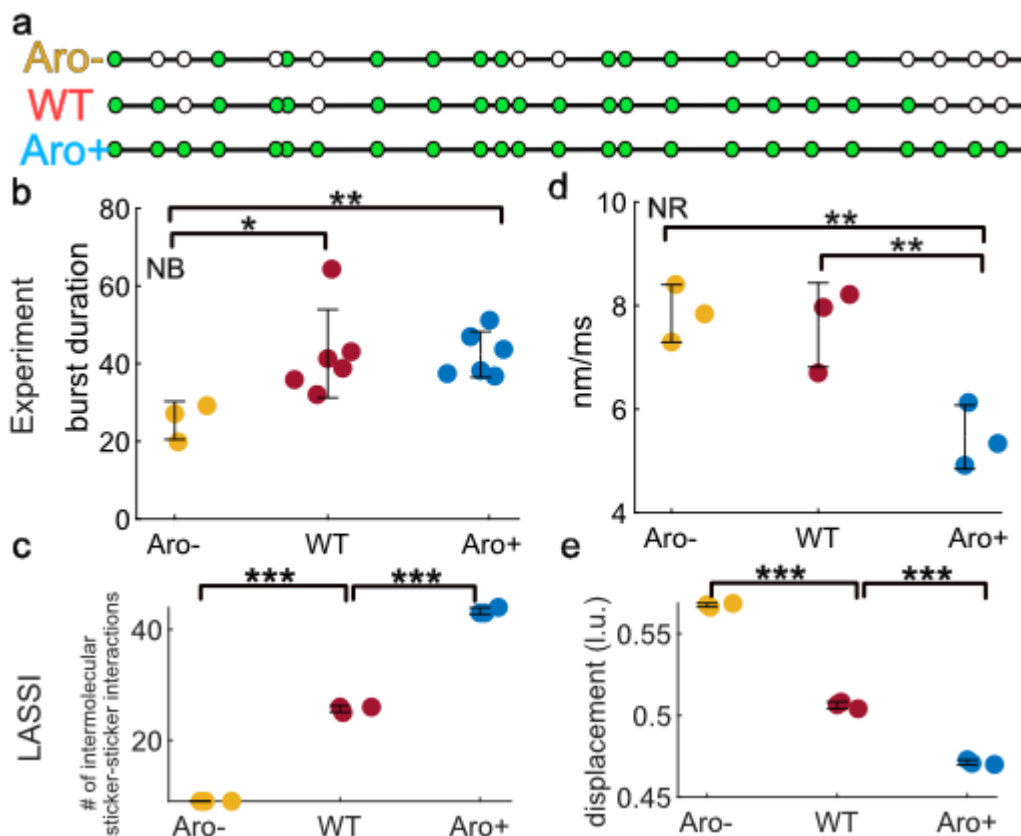
252

253   **Fig. 4. Nanoscale dynamics within condensates are influenced by the numbers of aromatic residues. a:**
254   Schematic showing the positions of aromatic amino acids as green circles in Aro$^-$, A1-LCD (WT), and Aro$^+$ variants.
255   **b**: Fluorescence burst durations for the three condensates measured using NB. **c**: Number of intermolecular sticker-
256   sticker interactions in simulated condensates. The sequence-specific simulations were performed using the LaSSI
257   engine. **d**: Speed of NR within condensates formed by Aro$^-$, WT, and Aro$^+$. **e**: Displacements of protein chains
258   quantified in simulated condensates. Circles in (b) represent the average burst durations of individual condensates,
259   and in (d-e) they represent the median values of measurement parameters for individual condensates. Error bar: mean
260   ± one standard deviation.

8

When probed using NB, the condensates formed by Aro$^+$ demonstrated the longest burst duration with an average of 43 ms. In contrast, when probed using NB, the condensates formed by Aro$^-$ show an average duration of 26 ms (**Fig. 4b**). Note that while dense phase concentrations of proteins change minimally within the condensates formed by different variants [2, 13, 28], the LaSSI simulations suggest that the extents of crosslinking vary with the valence of aromatic residues [13]. The simulations show that the numbers of sticker-sticker interactions are highest in those formed by Aro$^+$ and lowest in those formed by Aro$^-$ (**Fig. 4c**). Based on these comparisons, we infer that the longer burst durations for NB in Aro$^+$ condensates are due to the higher valence of aromatic residues. This larger valence results in higher extents of physical crosslinking and longer-lasting nanoscale hubs that trap NB for longer times and lead to longer fluorescence bursts. In contrast, condensates formed by Aro$^-$ feature fewer sticker-sticker interactions, and this leads to lower affinities and shorter burst durations when the condensates are probed using NB. Similar data were obtained when the condensates were probed using NR (**Extended Data Fig. 6**).

These dynamics can be probed by measuring the speeds of fluorogen displacements. The measured speeds serve as useful proxies for evaluating how crosslinks, which generate locally elastic networks [53], impede the mobilities of fluorogens. Our single-molecule tracking measurements indicate that NR moves fastest in Aro$^-$ condensates with an average speed of 8.9 nm/ms. In contrast, NR moves most slowly in Aro$^+$ condensates with an average speed of 6.7 nm/ms (**Fig. 4d**). These observations indicate that the extent of crosslinking engenders restrictions to the movements of fluorogens. These observations are in line with findings from LaSSI simulations, which show that proteins in Aro$^+$ condensates have the smallest displacements, whereas proteins in Aro$^-$ condensates have the largest displacements (**Fig. 4e** and **Extended Data Fig. 7**).

Single-molecule orientation localization microscopy reveals distinct features of interfaces.

The fluorescence of MC540 is influenced by the equilibrium between dimer and monomer states of MC540, where monomers are fluorescent and dimers are non-fluorescent [54]. This dimer-monomer equilibrium is strongly influenced by the molecular organization of the local environment [55]. We leveraged polarized epifluorescence microscopy to probe the orientational preferences sensed by this fluorogen. We separate the fluorescence emission from MC540 into x- and y-polarized channels (I_x, I_y). We then calculate the linear dichroism (LD) as the ratio: $(I_x - I_y)/(I_x + I_y)$, which takes values from –1 to +1. An LD near +1 signifies that the x-polarization dominates the fluorescence emission, whereas a negative LD near –1 indicates dominance of the y-polarization. We noticed that transitioning from Aro$^-$ to Aro$^+$, the condensates exhibit increasingly discernible pink and green hues at the interfaces of condensates, indicating a stronger polarization preference at the interface (**Fig. 5a**). For Aro$^+$, we observed mostly x-polarized fluorescence at the top and bottom edges and y-polarized fluorescence at the left and right sides (**Fig. 5a**). Comparing Aro$^+$ with Aro$^-$ and WT, we note that the LD distribution for Aro$^+$ is broader and encompasses more instances with large absolute LD values (**Fig. 5b**).

While SMLM images show a high density of MC540 at the interface of LCD condensates (**Fig. 5c**), they do not provide insights into how MC540 binds to the proteins. Thus, we employed single-molecule orientation localization microscopy (SMOLM) for measuring both the 3D position and orientation of MC540 (**Extended Data Fig. 8 and Movie S5**). SMOLM uses a pixOL phase mask to encode the information of 3D position and orientation into the images of single fluorogens [56]. We quantified orientational preferences by quantifying the angle, denoted as δ, of

305 MC540 in relation to the normal vector to the condensate interface (**Fig. 5d**). The SMOLM images,
306 color-coded according to δ and referred to as δ-SMOLM, indicate that freely diffusing MC540
307 dyes have a statistically significant preference for orientations parallel to the condensate interface
308 (depicted in bluish hues in **Fig. 5d**). This orientational preference is observed at the interfaces of
309 all three PLCD condensates (**Fig. 5d**). When comparing the median δ values across multiple
310 condensates for the three LCD variants, we observed that Aro$^+$ exhibits the highest δ value, with a
311 mean of 61°, while Aro$^-$ and WT have similar mean values of δ, which are 57° and 56°, respectively
312 (**Fig. 5e**).

313
314
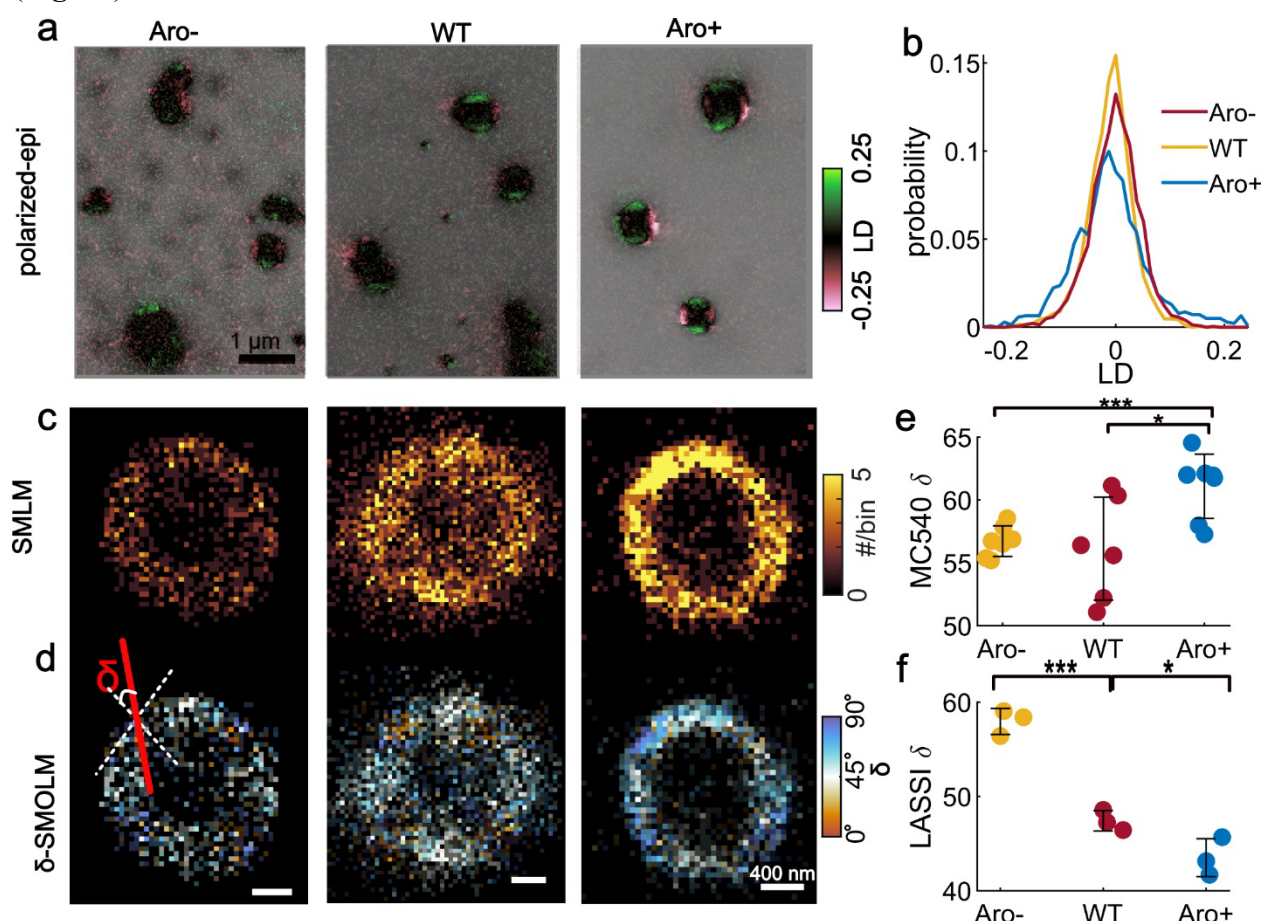
Fig. 5. MC540 preferentially localizes to interfaces and displays distinct orientational preferences. a: Linear
dichroism (LD) of MC540 measured by polarized epifluorescence imaging. **b:** LD distributions quantified from
images shown in (**a**). **c:** SMLM images of MC540. **d:** Orientation angles δ for MC540 measured with respect to the
normal vector to the condensate interface using SMOLM; the median angle δ is depicted within each 50 nm × 50 nm
bin. **e:** Median δ values computed across individual condensates (circles). Error bar: mean±1 standard deviation. **f:** δ
values computed from LaSSI simulations using orientations of protein molecules at the interface.

321 In line with recent work, MC540 may be viewed as an adsorbent, whereas the PLCD
322 molecules are the scaffolds [57]. Erkamp et al., recently showed that scaffolds show statistical
323 preference for orientations perpendicular to the plane of the interface, and adsorbents show a
324 statistical preference for orientations parallel to condensate interfaces [57]. Our SMOLM data for
325 MC540 are in line with this expectation. Unlike the adsorbents, scaffolds should have a statistical
326 preference for perpendicular orientations. This expectation was confirmed using results from

10

327 LaSSI simulations, which show that scaffold molecules have statistically smaller δ values **(Fig. 5f**
328 and **Extended Data Fig. 9)**. The observed orientational preferences become more pronounced as
329 the interactions among scaffolds become stronger with increasing numbers of aromatic residues
330 **(Fig. 5f)**. Taken together with the simulation results, the SMOLM data, obtained using MC540,
331 highlight the unique interfacial features of condensates.

Discussion

333 The picture that emerges from single fluorogen imaging may be summarized as follows
334 **(Fig. 6)**: The interiors of condensates are more hydrophobic than the coexisting dilute phases. This
335 is in line with recent inferences based on partitioning studies of small molecules that include drugs
336 and drug-like molecules [58]. Within condensates, we observe nanoscale spatial inhomogeneities
337 that are manifest as nanoscale hubs, because the fluorogens, particularly NR, bind preferentially
338 to hubs that are more hydrophobic than the background of the condensate. The nanoscale hubs
339 have a greater ability to trap fluorogens within their hydrophobic pockets, thus enabling them to
340 blink for longer times. Finally, SMOLM imaging suggests that the interface between dilute and
341 dense phases is a unique environment where MC540 molecules show marked orientational
342 preferences.
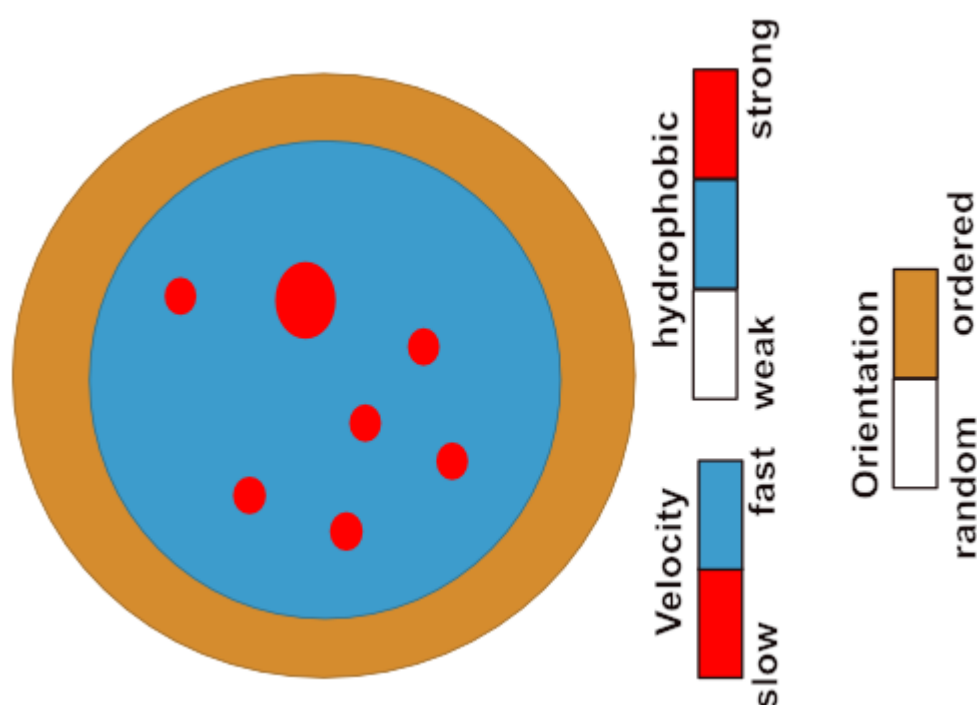
343
344 **Fig. 6. Schematic summarizing the structural features of condensates that were inferred from the fluorogenic**
345 **experiments.** Condensates are more hydrophobic than their coexisting dilute phases. They feature spatial
346 inhomogeneities that are manifest as nanoscale hubs (red regions). Hubs are more hydrophobic compared to other
347 regions (blue) within condensates, as well as to the dilute phase (white area). Fluorogens bound to nanoscale hubs
348 move more slowly compared to other regions. Proteins at the interface (orange) have distinct orientational preferences
349 that are unmasked by specific fluorogens such as MC540.

350 Other archetypes of low complexity domains that are drivers of condensate formation
351 include RG-rich IDRs such as the N-terminal domain from the RNA helicase DDX4 [3, 29]
352 **(Extended Data Fig. 10)**. Although the molecular grammars of RG-rich IDRs are different from

353 those of PLCDs [13], these domains appear to form condensates that respond in similar ways to NB
354 and NR. This similarity is not surprising given recent findings regarding the π-character of arginine
355 residues [59], and their apparent hydrophobicity [60] as probed by how water molecules organize
356 around arginine sidechains [61]. However, and in contrast to condensates formed by PLCDs and the
357 RG-rich IDR of DDX4, the condensates formed by polynucleotides such as poly-rA respond very
358 differently to NR (**Extended Data Fig. 10**). If there are spatial inhomogeneities and multiscale
359 hubs within RNA condensates, they are not sensed by NR. The implication is that different types
360 of fluorogens, specifically intercalating dyes, are needed to probe the internal organization of
361 RNA-rich condensates [57].

362 We have presented the first structural characterization of inhomogeneities within
363 condensates that leads to their descriptions as complex fluids with network-like structures [52].
364 Inhomogeneities observed in simulations [13] been mapped onto graph-theoretic approaches for
365 direct computations of condensate viscoelasticity [10, 62]. We directly measured the predicted spatial
366 and dynamical inhomogeneities within condensates. These observations help explain why
367 condensates are viscoelastic materials [5, 6, 7, 9, 10, 11, 30, 63, 64]. Continued development of new dye
368 functionalities [65, 66], imaging hardware [67], and analytical tools [68] will help with uncovering
369 spatiotemporal organization and dynamics within condensates, thus enabling direct assessments
370 of structure-function relationships of biomolecular condensates.

371 The existence of inhomogeneities, albeit on the micron-scale, has been well established for
372 multicomponent systems such as stress granules [69], nucleoli [70], nuclear speckles [71], the
373 mitochondrial nucleoid [4], and synthetic systems comprising two or more macromolecular
374 components [72, 73]. Our work highlights the existence of nanoscale spatial inhomogeneities for
375 condensates formed by a single type of macromolecule. We have shown how the varying stickers
376 affects the observed inhomogeneities. The spatial inhomogeneities give condensates a sponge-like
377 appearance. This is consistent with inferences made by Handwerger et al., who conjectured, based
378 on quantitative analysis of differential interference microscopy images, that membraneless nuclear
379 bodies including nucleoli, nuclear speckles, and Cajal bodies have sponge-like structures [74]. Our
380 findings suggest that multicomponent condensates that are characterized by micron-scale
381 inhomogeneities might also feature nanoscale inhomogeneities. Generalizing our methods to
382 characterize multicomponent systems is currently underway. To probe region-specific
383 inhomogeneities, this effort will require functionalizing the fluorogens with peptide-based probes
384 of molecular grammars that define distinct regions within larger, inhomogeneously organized
385 multicomponent condensates.

Acknowledgments

Author contributions

RVP and MDL conceived of and supervised the research. TW, MRK, and YQ designed and performed the imaging experiments and analyzed the data with inputs from MDL and RVP. MRK prepared A1-LCD, Aro⁺, Aro⁻, and DDX4 proteins, performed phase separation assays, and contributed intellectual insights. MF performed the LaSSI simulations and analyzed the simulation results. TW, MRK, MDL, and RVP wrote and edited the manuscript with input from all authors.

Competing interests

RVP is a member of the scientific advisory board of and shareholder at Dewpoint Therapeutics Inc. The work reported here was not influenced by this affiliation. The remaining authors have no competing interests to declare.

Additional information

Details of the imaging methods, analysis of images, constructs used, the preparation of condensates, LaSSI simulations, additional data and supplemental figures are presented in the supplementary material. Correspondence and requests for materials should be addressed to RVP and MDL.

References

1. Banani SF, Lee HO, Hyman AA, Rosen MK. Biomolecular condensates: organizers of cellular biochemistry. *Nature reviews Molecular cell biology* 2017, **18**(5)**:** 285-298.

2. Bremer A, Farag M, Borcherds WM, Peran I, Martin EW, Pappu RV*, et al.* Deciphering how naturally occurring sequence features impact the phase behaviours of disordered prion-like domains. *Nature Chemistry* 2022, **14:** 196-207.

3. Nott Timothy J, Petsalaki E, Farber P, Jervis D, Fussner E, Plochowietz A*, et al.* Phase Transition of a Disordered Nuage Protein Generates Environmentally Responsive Membraneless Organelles. *Molecular Cell* 2015, **57**(5)**:** 936-947.

4. Feric M, Sarfallah A, Dar F, Temiakov D, Pappu RV, Misteli T. Mesoscale structure–function relationships in mitochondrial transcriptional condensates. *Proceedings of the National Academy of Sciences* 2022, **119**(41)**:** e2207303119.

5. Jawerth L, Fischer-Friedrich E, Saha S, Wang J, Franzmann T, Zhang X*, et al.* Protein condensates as aging Maxwell fluids. *Science* 2020, **370**(6522)**:** 1317-1323.

6. Ghosh A, Kota D, Zhou H-X. Shear relaxation governs fusion dynamics of biomolecular condensates. *Nature Communications* 2021, **12**(1)**:** 5995.

7. Alshareedah I, Moosa MM, Pham M, Potoyan DA, Banerjee PR. Programmable Viscoelasticity in Protein-RNA Condensates with Disordered Sticker-Spacer Polypeptides. *Nature Communications* 2021, **12:** 6620.

8.   Feric M, Vaidya N, Harmon TS, Mitrea DM, Zhu L, Richardson TM*, et al.* Coexisting Liquid Phases Underlie Nucleolar Subcompartments. *Cell* 2016, **165**(7)**:** 1686-1697.

9.   Bergeron-Sandoval LP, Kumar S, Heris HK, Chang CLA, Cornell CE, Keller SL*, et al.* Endocytic proteins with prion-like domains form viscoelastic condensates that enable membrane remodeling. *Proceedings of the National Academy of Sciences* 2021, **118**(50)**:** e2113789118.

10. Alshareedah I, Borcherds W, M. , Cohen S, R. , Farag M, Singh A, Posey AE*, et al.* Sequence-specific interactions determine viscoelastic moduli and aging dynamics of protein condensates. *Nature Physics* 2023, **In press:** https://doi.org/10.1038/s41567-41024-02558-41561.

11. Wróbel JK, Cortez R, Fauci L. Modeling viscoelastic networks in Stokes flow. *Physics of Fluids* 2014, **26**(11)**:** 113102.

12. Michieletto D, Marenda M. Rheology and Viscoelasticity of Proteins and Nucleic Acids Condensates. *JACS Au* 2022, **2**(7)**:** 1506-1521.

13. Farag M, Cohen SR, Borcherds WM, Bremer A, Mittag T, Pappu RV. Condensates formed by prion-like low-complexity domains have small-world network structures and interfaces defined by expanded conformations. *Nature Communications* 2022, **13**(1)**:** 7722.

14. Farag M, Borcherds WM, Bremer A, Mittag T, Pappu RV. Phase separation of protein mixtures is driven by the interplay of homotypic and heterotypic interactions. *Nature Communications* 2023, **14**(1)**:** 5527.

15. Grimm JB, Heckman LM, Lavis LD. Chapter One - The Chemistry of Small-Molecule Fluorogenic Probes. In: Morris MC (ed). *Progress in Molecular Biology and Translational Science*, vol. 113. Academic Press, 2013, pp 1-34.

16. Martinez V, Henary M. Nile Red and Nile Blue: Applications and Syntheses of Structural Analogues. *Chemistry – A European Journal* 2016, **22**(39)**:** 13764-13782.

17. Verkman AS. Mechanism and kinetics of merocyanine 540 binding to phospholipid membranes. *Biochemistry* 1987, **26**(13)**:** 4050-4056.

18. Li H, Vaughan JC. Switchable Fluorophores for Single-Molecule Localization Microscopy. *Chemical Reviews* 2018, **118**(18)**:** 9412-9454.

19. Lew MD, Lee SF, Ptacin JL, Lee MK, Twieg RJ, Shapiro L, *et al.* Three-dimensional superresolution colocalization of intracellular protein superstructures and the cell surface in live Caulobacter crescentus. *Proceedings of the National Academy of Sciences* 2011, **108**(46)**:** E1102-E1110.

20. Spehar K, Ding T, Sun Y, Kedia N, Lu J, Nahass GR, *et al.* Super-resolution Imaging of Amyloid Structures over Extended Times by Using Transient Binding of Single Thioflavin T Molecules. *ChemBioChem* 2018, **19**(18)**:** 1944-1948.

21. Danylchuk DI, Moon S, Xu K, Klymchenko AS. Switchable Solvatochromic Probes for Live-Cell Super-resolution Imaging of Plasma Membrane Organization. *Angewandte Chemie International Edition* 2019, **58**(42)**:** 14920-14924.

22. Ding T, Wu T, Mazidi H, Zhang O, Lew MD. Single-molecule orientation localization microscopy for resolving structural heterogeneities between amyloid fibrils. *Optica* 2020, **7**(6)**:** 602-607.

23. Lu J, Mazidi H, Ding T, Zhang O, Lew MD. Single-Molecule 3D Orientation Imaging Reveals Nanoscale Compositional Heterogeneity in Lipid Membranes. *Angewandte Chemie International Edition* 2020, **59**(40)**:** 17572-17579.

24. Klymchenko AS. Solvatochromic and Fluorogenic Dyes as Environment-Sensitive Probes: Design and Biological Applications. *Accounts of Chemical Research* 2017, **50**(2)**:** 366-375.

25. Hou Y, Bardo AM, Martinez C, Higgins DA. Characterization of Molecular Scale Environments in Polymer Films by Single Molecule Spectroscopy. *The Journal of Physical Chemistry B* 2000, **104**(2)**:** 212-219.

26. Sackett DL, Knutson JR, Wolff J. Hydrophobic surfaces of tubulin probed by time-resolved and steady-state fluorescence of nile red. *Journal of Biological Chemistry* 1990, **265**(25)**:** 14899-14906.

27. Tajalli H, Gilani AG, Zakerhamidi MS, Tajalli P. The photophysical properties of Nile red and Nile blue in ordered anisotropic media. *Dyes and Pigments* 2008, **78**(1)**:** 15-24.

28. Martin EW, Holehouse AS, Peran I, Farag M, Incicco JJ, Bremer A, *et al.* Valence and patterning of aromatic residues determine the phase behavior of prion-like domains. *Science* 2020, **367**(6478)**:** 694-699.

29. Brady JP, Farber PJ, Sekhar A, Lin Y-H, Huang R, Bah A, *et al.* Structural and hydrodynamic properties of an intrinsically disordered region of a germ cell-specific

protein on phase separation. *Proceedings of the National Academy of Sciences USA* 2017, **114**(39)**:** E8194-E8203.

30.   Alshareedah I, Kaur T, Banerjee PR. Methods for characterizing the material properties of biomolecular condensates. *Methods in Enzymology* 2021, **646:** 143-183.

31.   Kaur T, Raju M, Alshareedah I, Davis RB, Potoyan DA, Banerjee PR. Sequence-encoded and composition-dependent protein-RNA interactions control multiphasic condensate morphologies. *Nature Communications* 2021, **12**(1)**:** 872.

32.   Shillcock JC, Lagisquet C, Alexandre J, Vuillon L, Ipsen JH. Model biomolecular condensates have heterogeneous structure quantitatively dependent on the interaction profile of their constituent macromolecules. *Soft Matter* 2022**:** 10.1039/D1032SM00387B.

33.   Böddeker TJ, Rosowski KA, Berchtold D, Emmanouilidis L, Han Y, Allain FHT*, et al.* Non-specific adhesive forces between filaments and membraneless organelles. *Nature Physics* 2022, **18**(5)**:** 571-578.

34.   King MR, Ruff KM, Lin AZ, Pant A, Farag M, Lalmansingh JM*, et al.* Macromolecular condensation organizes nucleolar sub-phases to set up a pH gradient. *Cell* 2024, **187**(8)**:** 1889-1906.e1824.

35.   Sharonov A, Hochstrasser RM. Wide-field subdiffraction imaging by accumulated binding of diffusing probes. *Proceedings of the National Academy of Sciences* 2006, **103**(50)**:** 18911-18916.

36.   Ruff KM, Dar F, Pappu RV. Ligand effects on phase separation of multivalent macromolecules. *Proceedings of the National Academy of Sciences USA* 2021, **118**(10)**:** e2017184118.

37.   Ruff KM, Dar F, Pappu RV. Polyphasic linkage and the impact of ligand binding on the regulation of biomolecular condensates. *Biophysics Reviews* 2021, **2**(2)**:** 021302.

38.   Kuo C, Hochstrasser RM. Super-resolution Microscopy of Lipid Bilayer Phases. *Journal of the American Chemical Society* 2011, **133**(13)**:** 4664-4667.

39.   Lelek M, Gyparaki MT, Beliu G, Schueder F, Griffié J, Manley S*, et al.* Single-molecule localization microscopy. *Nature Reviews Methods Primers* 2021, **1**(1)**:** 39.

16

40. Betzig E, Patterson GH, Sougrat R, Lindwasser OW, Olenych S, Bonifacino JS, *et al.* Imaging Intracellular Fluorescent Proteins at Nanometer Resolution. *Science* 2006, **313**(5793)**:** 1642-1645.

41. Hess ST, Girirajan TPK, Mason MD. Ultra-High Resolution Imaging by Fluorescence Photoactivation Localization Microscopy. *Biophysical Journal* 2006, **91**(11)**:** 4258-4272.

42. Rust MJ, Bates M, Zhuang X. Sub-diffraction-limit imaging by stochastic optical reconstruction microscopy (STORM). *Nature Methods* 2006, **3**(10)**:** 793-796.

43. Chhabra R. Nonwoven Uniformity — Measurements Using Image Analysis. *International Nonwovens Journal* 2003, **os-12**(1)**:** 1558925003os-1551200112.

44. Leibler L. Theory of Microphase Separation in Block Copolymers. *Macromolecules* 1980, **13**(6)**:** 1602-1617.

45. Ripley BD. Modelling Spatial Patterns. *Journal of the Royal Statistical Society: Series B (Methodological)* 1977, **39**(2)**:** 172-192.

46. Khater IM, Nabi IR, Hamarneh G. A Review of Super-Resolution Single-Molecule Localization Microscopy Cluster Analysis and Quantification Methods. *Patterns* 2020, **1**(3).

47. Malkusch S, Endesfelder U, Mondry J, Golléri M, Verveer PJ, Heilemann M. Coordinate-based colocalization analysis of single-molecule localization microscopy data. *Histochemistry and Cell Biology* 2012, **137**(1)**:** 1-10.

48. Shen M, Ding T, Hartman ST, Wang F, Krucylak C, Wang Z, *et al.* Nanoscale Colocalization of Fluorogenic Probes Reveals the Role of Oxygen Vacancies in the Photocatalytic Activity of Tungsten Oxide Nanowires. *ACS Catalysis* 2020, **10**(3)**:** 2088-2099.

49. Pappu RV, Cohen SR, Dar F, Farag M, Kar M. Phase Transitions of Associative Biomacromolecules. *Chemical Reviews* 2023, **123**(14)**:** 8945-8987.

50. Mittag T, Pappu RV. A conceptual framework for understanding phase separation and addressing open questions and challenges. *Molecular Cell* 2022, **82**(12)**:** 2201-2214.

51. Shen Z, Jia B, Xu Y, Wessén J, Pal T, Chan HS*, et al.* Biological condensates form percolated networks with molecular motion properties distinctly different from dilute solutions. *eLife* 2023, **12:** e81907.

52. Dar F, Cohen SR, Mitrea DM, Phillips AH, Nagy G, Leite WC*, et al.* Biomolecular condensates form spatially inhomogeneous network fluids. *Nature Communications* 2024, **15**(1)**:** 3413.

53. Weeks ER, Weitz DA. Properties of Cage Rearrangements Observed near the Colloidal Glass Transition. *Physical Review Letters* 2002, **89**(9)**:** 095704.

54. Kulinich AV, Aleksandr AI. Merocyanine dyes: synthesis, structure, properties and applications. *Russian Chemical Reviews* 2009, **78**(2)**:** 141.

55. Stillwell W, Wassall SR, Dumaual AC, Ehringer WD, Browning CW, Jenski LJ. Use of merocyanine (MC540) in quantifying lipid domains and packing in phospholipid vesicles and tumor cells. *Biochimica et Biophysica Acta (BBA) - Biomembranes* 1993, **1146**(1)**:** 136-144.

56. Wu T, Lu J, Lew MD. Dipole-spread-function engineering for simultaneously measuring the 3D orientations and 3D positions of fluorescent molecules. *Optica* 2022, **9**(5)**:** 505-511.

57. Erkamp NA, Farag M, Qiu Y, Qian D, Sneideris T, Wu T*, et al.* Differential interactions determine anisotropies at interfaces of RNA-based biomolecular condensates. *bioRxiv* 2024**:** 2024.2008.2019.608662.

58. Thody SA, Clements H, D, Baniasadi H, Lyon A, S, Sigman M, S., Rosen M, K. Small Molecule Properties Define Partitioning into Biomolecular Condensates. *bioRxiv* 2022**:** 2022.2012.2019.521099.

59. Vernon RM, Chong PA, Tsang B, Kim TH, Bah A, Farber P*, et al.* Pi-Pi contacts are an overlooked protein feature relevant to phase separation. *eLife* 2018, **7:** e31486.

60. Hong Y, Najafi S, Casey T, Shea J-E, Han S-I, Hwang DS. Hydrophobicity of arginine leads to reentrant liquid-liquid phase separation behaviors of arginine-rich proteins. *Nature Communications* 2022, **13**(1)**:** 7326.

61. Fossat MJ, Zeng X, Pappu RV. Uncovering Differences in Hydration Free Energies and Structures for Model Compound Mimics of Charged Side Chains of Amino Acids. *The Journal of Physical Chemistry B* 2021, **125**(16)**:** 4148-4161.

18

634

635 62. Cohen SR, Banerjee PR, Pappu RV. Direct computations of viscoelastic moduli of
636 biomolecular condensates. *The Journal of Chemical Physics* 2024, **In press:**
637 https://doi.org/10.1101/2024.1106.1111.598543.

638

639 63. Zhou H-X. Viscoelasticity of biomolecular condensates conforms to the Jeffreys model.
640 *The Journal of Chemical Physics* 2021, **154**(4)**:** 041103.

641

642 64. Alshareedah I, Singh A, Yang S, Ramachandran V, Quinn A, Potoyan DA*, et al.*
643 Determinants of viscoelasticity and flow activation energy in biomolecular condensates.
644 *Science Advances* 2024, **10**(7)**:** eadi6539.

645

646 65. Needham L-M, Weber J, Varela JA, Fyfe JWB, Do DT, Xu CK*, et al.* ThX – a next-
647 generation probe for the early detection of amyloid aggregates. *Chemical Science* 2020,
648 **11**(18)**:** 4578-4583.

649

650 66. Aparin IO, Yan R, Pelletier R, Choi AA, Danylchuk DI, Xu K*, et al.* Fluorogenic Dimers
651 as Bright Switchable Probes for Enhanced Super-Resolution Imaging of Cell Membranes.
652 *Journal of the American Chemical Society* 2022, **144**(39)**:** 18043-18053.

653

654 67. Zhang O, Guo Z, He Y, Wu T, Vahey MD, Lew MD. Six-dimensional single-molecule
655 imaging with isotropic resolution using a multi-view reflector microscope. *Nature*
656 *Photonics* 2023, **17:** 179-186.

657

658 68. Schröder T, Bohlen J, Ochmann SE, Schüler P, Krause S, Lamb DC*, et al.* Shrinking gate
659 fluorescence correlation spectroscopy yields equilibrium constants and separates
660 photophysics from structural dynamics. *Proceedings of the National Academy of Sciences*
661 2023, **120**(4)**:** e2211896120.

662

663 69. Jain S, Wheeler Joshua R, Walters Robert W, Agrawal A, Barsic A, Parker R. ATPase-
664 Modulated Stress Granules Contain a Diverse Proteome and Substructure. *Cell* 2016,
665 **164**(3)**:** 487-498.

666

667 70. Pederson T. The Nucleolus. *Cold Spring Harbor Perspectives in Biology* 2011, **3**(3).

668

669 71. Fei J, Jadaliha M, Harmon TS, Li IT, Hua B, Hao Q*, et al.* Quantitative analysis of
670 multilayer organization of proteins and RNA in nuclear speckles at super resolution.
671 *Journal of Cell Science* 2017, **130**(24)**:** 4180-4192.

672

673   72.   Simon JR, Carroll NJ, Rubinstein M, Chilkoti A, López GP. Programming molecular self-
674   assembly of intrinsically disordered proteins containing sequences of low complexity.
675   *Nature Chemistry* 2017, **9**(6)**:** 509-515.

676
677   73.   Harmon TS, Holehouse AS, Pappu RV. Differential solvation of intrinsically disordered
678   linkers drives the formation of spatially organized droplets in ternary systems of linear
679   multivalent proteins. *New Journal of Physics* 2018, **20**(4)**:** 045002.

680
681   74.   Handwerger KE, Cordero JA, Gall JG. Cajal Bodies, Nucleoli, and Speckles in the
682   Xenopus Oocyte Nucleus Have a Low-Density, Sponge-like Structure. *Molecular Biology*
683   *of the Cell* 2005, **16**(1)**:** 202-211.

684

685

686

687

688

Extended Data Figures for:

Single fluorogen imaging reveals distinct environmental and structural features of biomolecular condensates

Authors: Tingting Wu[1,2,4], Matthew R. King[2,3,4], Yuanxin Qiu[1,2], Mina Farag[2,3], Rohit V. Pappu[2,3*], Matthew D. Lew[1,2*]

Affiliations:

[1] Department of Electrical and Systems Engineering, Washington University in St. Louis, James F. McKelvey School of Engineering, Washington University in St. Louis; St. Louis, MO 63130, USA.

[2] Center for Biomolecular Condensates, James F. McKelvey School of Engineering, Washington University in St. Louis; St. Louis, MO 63130, USA.

[3] Department of Biomedical Engineering, Washington University in St. Louis, James F. McKelvey School of Engineering, Washington University in St. Louis; St. Louis, MO 63130, USA.

[4]These authors contributed equally: Tingting Wu, Matthew R. King

Corresponding authors. Email: pappu@wustl.edu; mdlew@wustl.edu
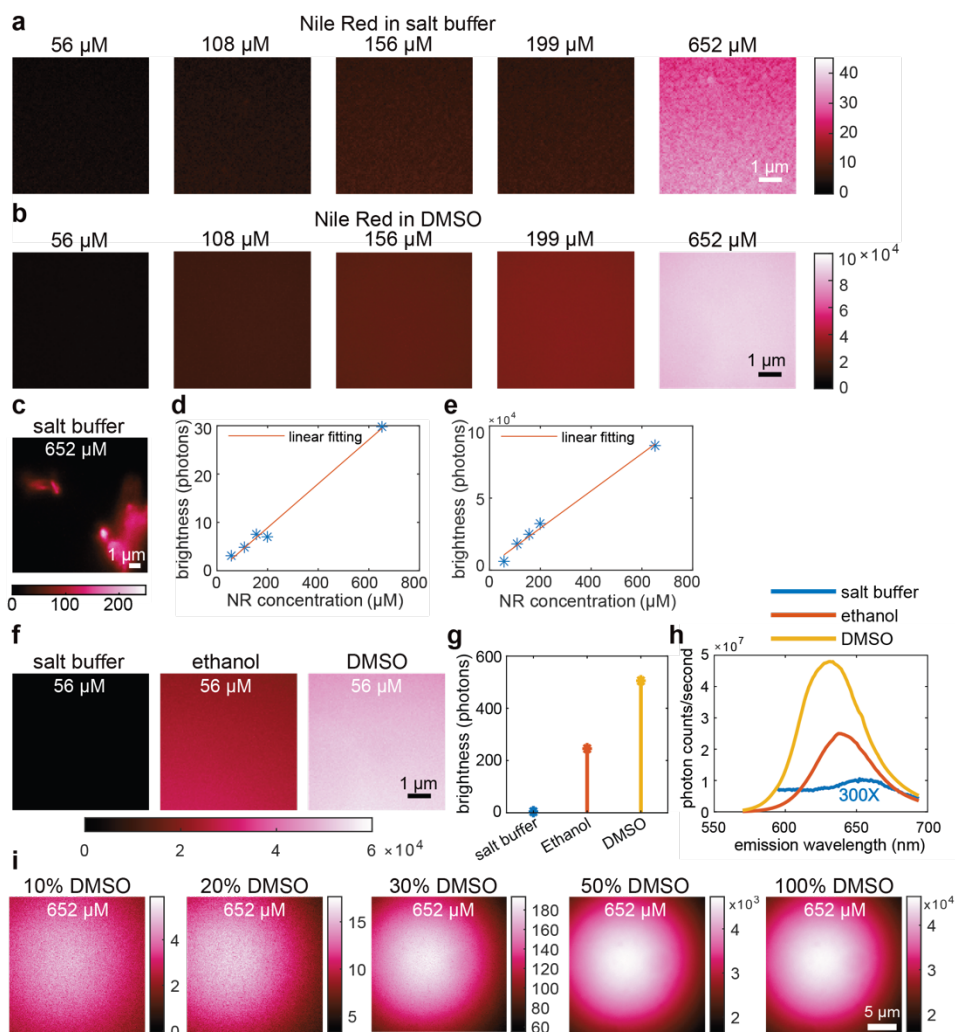
Extended Data Fig. 1. Calibration of the NR dye in homogeneous solutions. **a**: The intensity of NR at different concentrations dissolved in an aqueous buffer comprising 20 mM HEPES with 300 mM NaCl. This buffer is identical to the one used for preparing A1-LCD condensates. Images were captured with the microscope focused on the coverslip. Note that the intensity increases with NR concentration. **b**: Intensity of NR at different concentrations dissolved in DMSO. Images were captured on the coverslip. The intensity increases with NR concentration. Comparing panels in **a** to panels in **b**, we see that at equivalent concentrations of NR, the intensities in DMSO are at least three orders of magnitude higher than in aqueous buffers. **c**: In aqueous buffers, molecules of NR form aggregates at or above concentrations of 652 µM. This image is captured above the coverslip. The morphologies of NR aggregates are different from the hubs we observed in condensates. **d**: and **e**: There is a linear correspondence between brightness, quantified in terms of the number of photons collected, and the concentration of fluorogens we use, both in aqueous buffers (d) and in DMSO (e). **f**: Fluorescence intensity of 56 µm NR solutions in different solvents. These measurements highlight the increased brightness of the solvatochromic NR as the hydrophobicity of the solvent increases. Calibration of the increase in fluorescence intensities is provided by the color bar. **g**: The data in (**f**) are summarized by plotting the average intensities of the images. **h**: The emission spectrum of NR in three different solvents. The emission spectrum of NR in the aqueous buffer is scaled by a factor of 300 for better visualization. The emission spectrum of NR is blue-shifted as the hydrophobicity of the solvent increases. **i**: The dielectric constant of 100% DMSO is 46.7 and that of aqueous solutions is ~78 at 296 K. At high concentrations of NR (652 µM), we quantified the fluorescence intensity as a function of % DMSO. These measurements show that the aggregates present in aqueous buffers (0% DMSO) are absent even in the presence of 10% DMSO. As the % of DMSO increases, the NR intensity increases by 2-4 orders of magnitude, thus highlighting the fluorogenic nature of NR.

ED-2
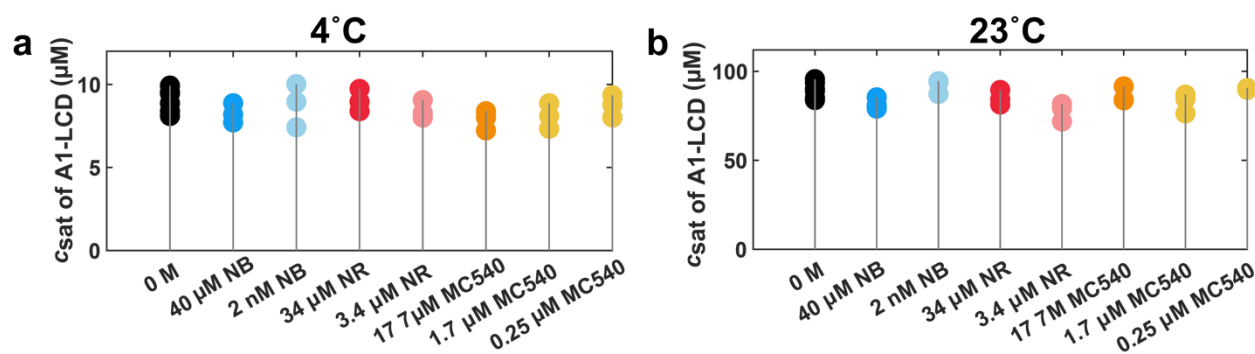
Extended Data Fig. 2. Quantifying the effects of different fluorogens on the driving forces for phase separation. Driving forces were quantified by measuring saturation concentrations (c_{sat}) of A1-LCD molecules in the presence of different amounts of the different fluorogens used in this work. Within the error of the measurements, we find that adding NR, NB, and MC540 at different concentrations have minimal effects on the measured values of c_{sat}. This inference is made based on comparisons to measurements made in the absence of dyes (black circles). All measurements were performed using a starting concentration of 150 µM A1-LCD in 20 mM HEPES buffer and 300 mM NaCl at (**a**) 4 °C and (**b**) 23 °C. Prepared protein and dye mixtures were allowed to phase separate for 30 minutes at the indicated temperatures before the dilute phase was separated from the dense phase via centrifugation and protein concentration measured using absorbance at 280 nm. Each set of samples was prepared in triplicate and measured independently; each triplicate measurement is shown as individual filled circles.
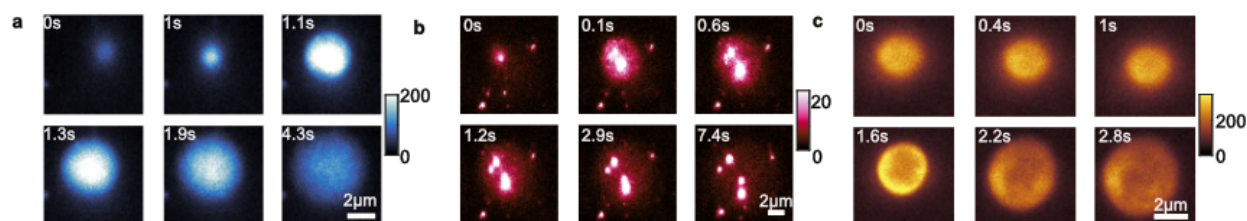

Extended Data Fig. 3. Dynamic wetting of the glass coverslip by A1-LCD condensates. The images were captured using (**a**) NB, (**b**) NR, and (**c**) MC540.

ED-3
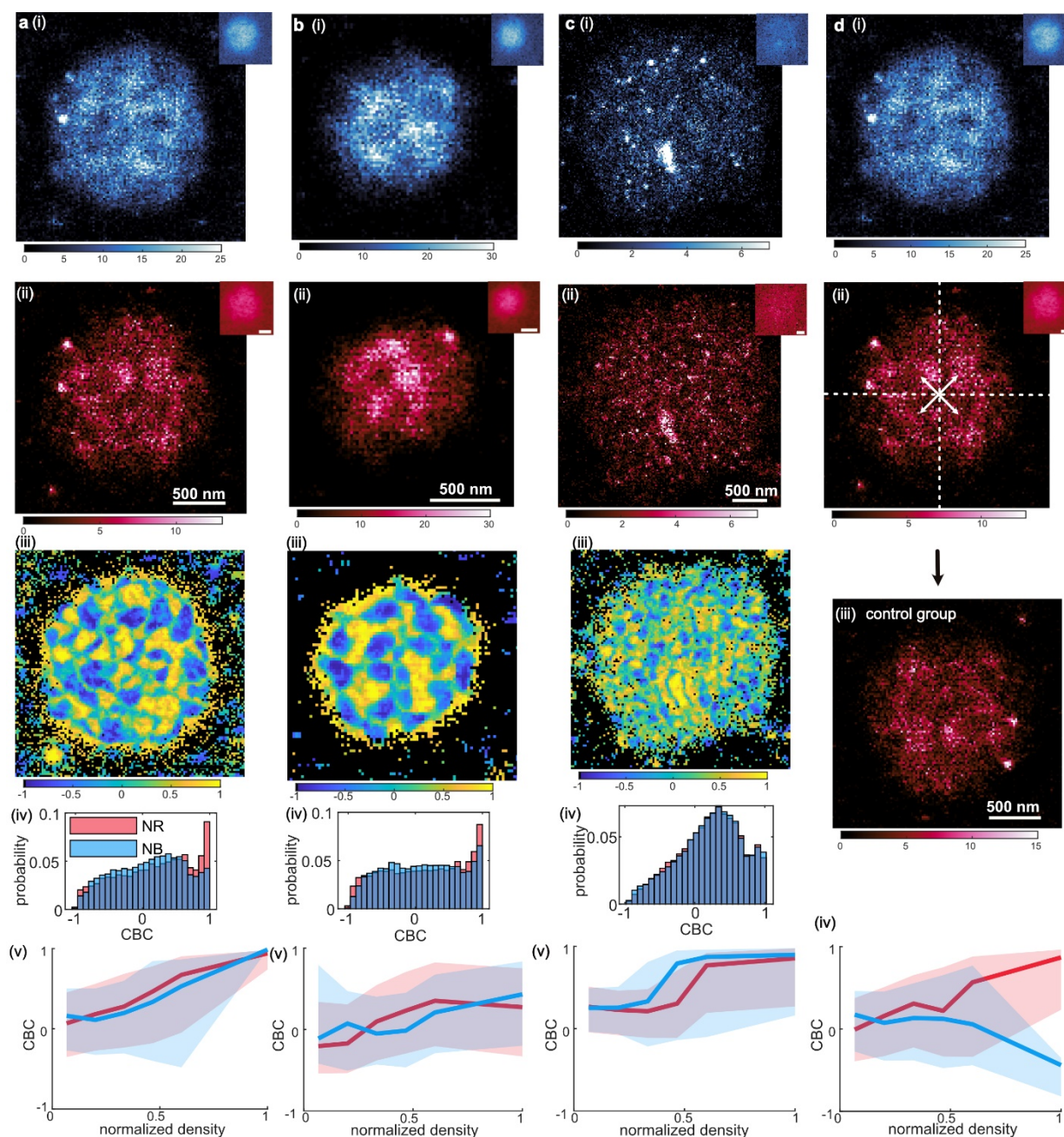
Extended Data Fig. 4. Spatial inhomogeneities within A1-LCD condensates imaged by NB and NR are highly correlated. **a**, **b**, and **c**: Correlation between NB and NR measured for three different A1-LCD condensates. SMLM images of single condensates collected using (i) NB and (ii) NR. Insets: epifluorescence images. Color bars: number of single molecules within each 20 nm × 20 nm bin. (iii) Coordinate-based correlation (CBC) between NR and NB localizations averaged for localizations within each 20 nm × 20 nm bin. (iv) Distribution of CBC scores for (blue) NB and (red) NR. (v) CBC of NB (blue) and NR (red) plotted as a function of localization density. Solid lines: median value; shaded area: 25th-75th percentile. **d:** A condensate measured using (i) NB and (ii) NR as shown in **a**. We swapped emitters in the four regions of (ii) to form (iii) a modified NR condensate that should have weak correlations with the original condensate in **a**. (iv) CBC values between (i) NB localizations and (iii) the modified NR localizations.

ED-4
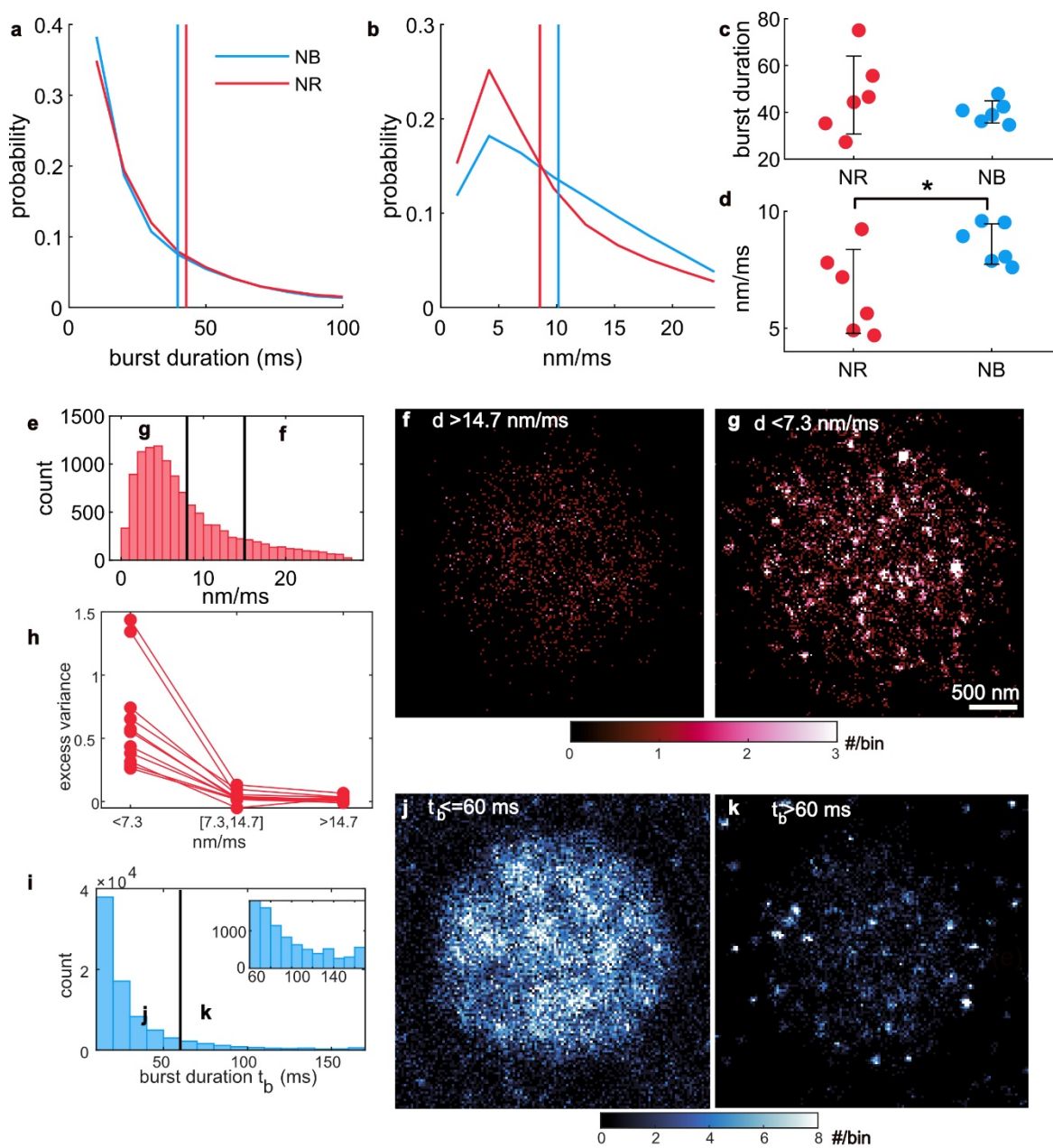
Extended Data Fig. 5. Tracking single-molecule fluorescence bursts and speeds reveal inhomogeneous molecular distributions within A1-LCD condensates. a, b: Distribution of (**a**) burst durations and (**b**) speeds for NB (blue) and NR (red). **c**: Mean burst duration for individual condensates. **d**: Median speed for fluorogens within individual condensates. Error bar: mean±1 standard deviation. Single-molecule tracking of (**e-h**) NR and (**i-k**) NB. **e:** NR speeds measured between consecutive camera frames (10 ms exposure time). **f, g:** SMLM images of NR with speeds (**f**) larger than 14.7 nm/ms and (**g**) shorter than 7.3 nm/ms. **h**: Excess variance of NR localizations grouped by speed (left: ≤ 7.3 nm/ms, middle: between 7.3/ms and 14.7 nm/ms, right: >14.7 nm/ms). Lines: excess variance of molecules within each condensate. **i:** Fluorescence burst durations t_b of NB. **j, k:** SMLM images of fluorogens (NB) with burst durations (**j**) shorter than 60 ms and (**k**) longer than 60 ms.

ED-5
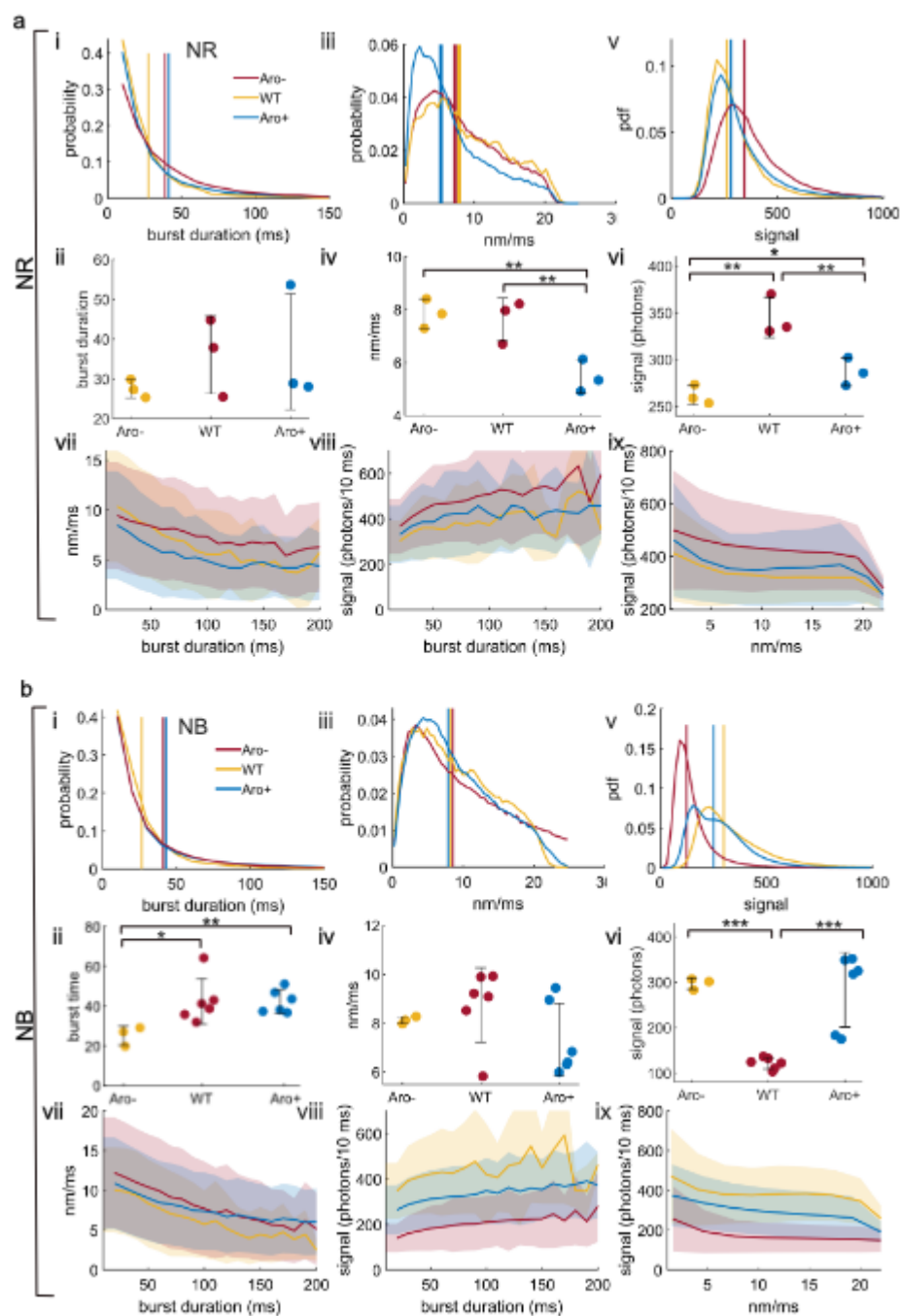
Extended Data Fig. 6. Speeds and burst durations of NR and NB molecules within Aro⁻, WT, and Aro⁺ condensates. a, b: Measurements of (a) NR and (b) NB for three different LCDs. **i,** Distribution of burst duration. Vertical lines: mean burst durations. **ii,** Mean burst duration for individual condensates. **iii,** Distribution of speed. Vertical lines: median speeds. **iv,** Median speed for individual condensates. **v,** Distribution of signal photons. Vertical lines: median signals. **vi,** Median signal of SMs in individual condensates. Error bar: mean±1 standard deviation. **vii,** Speeds of SMs as a function of their burst durations. **viii,** Signal photons of SMs as a function of their burst durations. **ix,** Signal photons as a function of their speed. Shaded region: ±1 standard deviation.
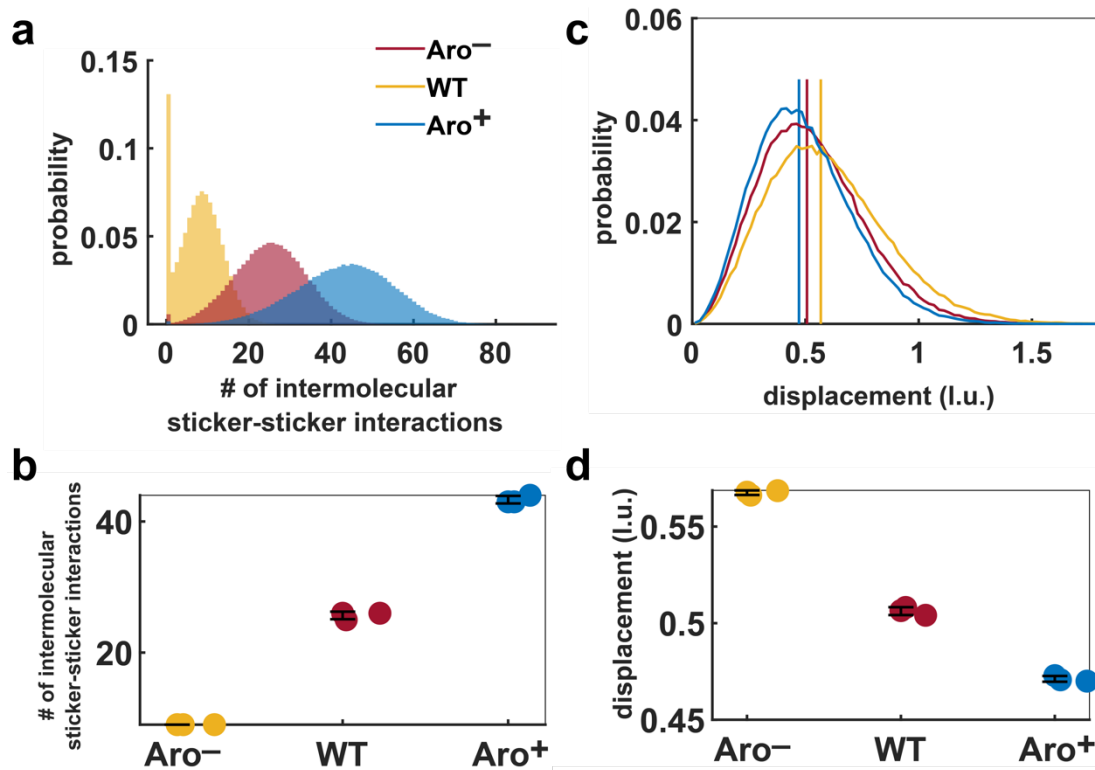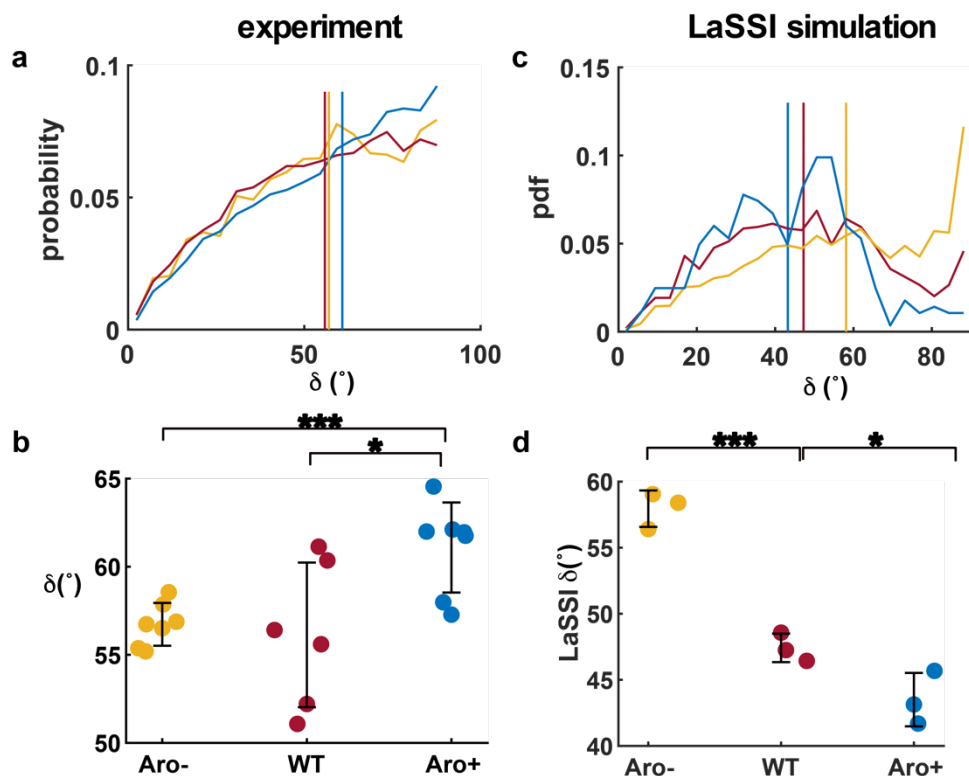
Extended Data Fig. 7. LaSSI simulations of condensates formed by Aro⁻, WT, and Aro⁺. a: Distribution of the number of sticker-sticker interactions. **b**: The median number of sticker-sticker interactions within individual condensates (reproduced from Fig. 4c). **c**: Distribution of displacement of protein chains. Vertical lines are the median displacements in lattice units (l.u). **d**: The median displacement of protein chains (reproduced from Fig. 4e). Error bars: mean±1 standard deviation.
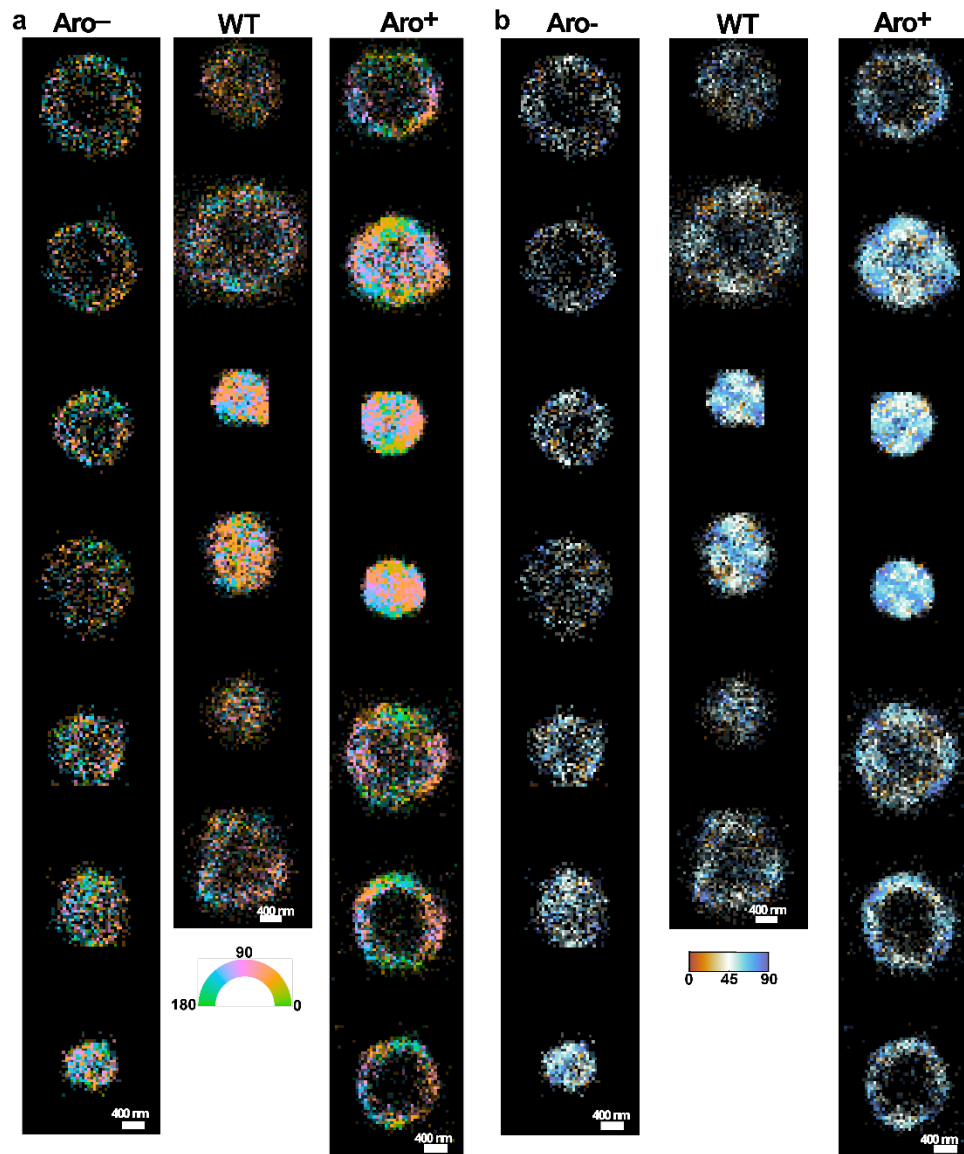
Extended Data Fig. 8. Single-molecule orientation-localization microscopy (SMOLM) of Aro-, WT, Aro+ condensates. a: Single-molecule orientation image with colors representing the measured azimuthal angles φ in the xy-plane. **b:** Single-molecule orientation image with colors representing the orientation angle δ measured with respect to the normal vector to the condensate interface. The images are reconstructed from localizations of freely diffusing MC540.

Extended Data Fig. 9. Orientation of MC540 measured by SMOLM and orientation of protein chains quantified in LaSSI simulations of different condensates. a: Distribution of the orientation angle δ for MC540 measured with respect to the normal vector to the condensate interface using SMOLM. Vertical lines: median value of orientation δ. **b**: The median orientation δ of MC540 within individual condensates (reproduced from Fig. 5e). **c**: Distribution of orientation δ of protein chains in LaSSI simulations. Vertical lines: median orientation δ. **d**: The median orientation δ of protein chains (reproduced from Fig. 5f). Error bar: mean$\pm$1 standard deviation.

ED-9
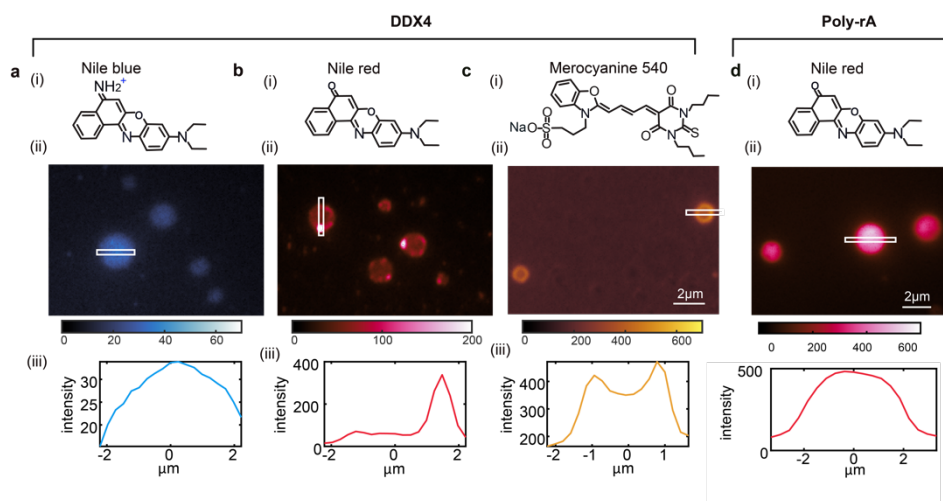
Extended Data Fig. 10. Epifluorescence microscopy reveals that different fluorogenic probes sense chemical environments inside DDX4-IDR condensates from different perspectives. Imaging DDX4-IDR condensates using **a.** Nile blue (NB), **b.** Nile red (NR), and **c.** merocyanine 540 (MC540). (i) Chemical structures. (ii) Typical condensates as viewed by epifluorescence microscopy. (iii) Fluorescence intensity profiles along the long axis of white box shown in (ii). **d**. Imaging poly-rA condensates using NR.